

MIT Open Access Articles

SD 1313-0019: ANOTHER SECOND-GENERATION STAR WITH [Fe/H] = -5.0, OBSERVED WITH THE MAGELLAN TELESCOPE

The MIT Faculty has made this article openly available. **Please share** how this access benefits you. Your story matters.

Citation: Frebel, Anna, Anirudh Chiti, Alexander P. Ji, Heather R. Jacobson, and Vinicius M. Placco. "SD 1313-0019: ANOTHER SECOND-GENERATION STAR WITH [Fe/H] = -5.0, OBSERVED WITH THE MAGELLAN TELESCOPE." *The Astrophysical Journal* 810, no. 2 (September 9, 2015): L27. © 2015 The American Astronomical Society

As Published: <http://dx.doi.org/10.1088/2041-8205/810/2/L27>

Publisher: IOP Publishing

Persistent URL: <http://hdl.handle.net/1721.1/100051>

Version: Final published version: final published article, as it appeared in a journal, conference proceedings, or other formally published context

Terms of Use: Article is made available in accordance with the publisher's policy and may be subject to US copyright law. Please refer to the publisher's site for terms of use.



SD 1313–0019: ANOTHER SECOND-GENERATION STAR WITH $[\text{Fe}/\text{H}] = -5.0$, OBSERVED WITH THE *MAGELLAN* TELESCOPE*

ANNA FREBEL^{1,2}, ANIRUDH CHITI¹, ALEXANDER P. JI¹, HEATHER R. JACOBSON¹, AND VINICIUS M. PLACCO^{3,2}

¹Department of Physics and Kavli Institute for Astrophysics and Space Research, Massachusetts Institute of Technology, Cambridge, MA 02139, USA

²Joint Institute for Nuclear Astrophysics–Center for Evolution of the Elements, East Lansing, MI 48824, USA

³Department of Physics, University of Notre Dame, Notre Dame, IN 46556, USA

Received 2015 June 28; accepted 2015 August 18; published 2015 September 9

ABSTRACT

We present a *Magellan*/MIKE high-resolution ($R \sim 35,000$) spectrum of the ancient star SD 1313–0019, which has an iron abundance of $[\text{Fe}/\text{H}] = -5.0$, paired with a carbon enhancement of $[\text{C}/\text{Fe}] \sim 3.0$. The star was initially identified by Allende Prieto et al. in the BOSS survey. Its medium-resolution spectrum suggested a higher metallicity of $[\text{Fe}/\text{H}] = -4.3$ due to the Ca II K line blending with a CH feature, which is a common issue related to the search for the most iron-poor stars. This star joins several other similar stars with $[\text{Fe}/\text{H}] \lesssim -5.0$ that all display a combination of low-iron and high-carbon abundances. Other elemental abundances of SD 1313–0019 follow that of more metal-rich halo stars. Fitting the abundance pattern with yields of Population III supernovae suggests that SD 1313–0019 had only one massive progenitor star with $20\text{--}30 M_{\odot}$ that must have undergone a mixing and fallback episode. Overall, there are now five stars known with $[\text{Fe}/\text{H}] \lesssim -5.0$ (1D local thermodynamic equilibrium abundances). This ever-increasing population of carbon-rich, iron-deficient stars can potentially constrain nucleosynthesis in Population III stars and their supernova explosions, the formation mechanisms of the first low-mass stars, and the nature of the first galaxies.

Key words: early universe – Galaxy: halo – stars: abundances – stars: individual (SD 1313–0019) – stars: Population II

1. INTRODUCTION

The chemical abundances of the most iron-poor stars provide a record of the nucleosynthesis yields of the first stars that formed in the universe. By now, ~ 20 Milky Way halo stars are known with $[\text{Fe}/\text{H}] \lesssim -4.0$ (see, e.g., Frebel & Norris 2015; Placco et al. 2015), of which five have $[\text{Fe}/\text{H}] \lesssim -5.0$ (Christlieb et al. 2002; Frebel et al. 2005; Caffau et al. 2011; Keller et al. 2014; Bonifacio et al. 2015). They are thought to be second-generation stars from the early universe with just one massive Population III (hereafter Pop III) first star progenitor that produced the chemical elements that we can still observe in their stellar atmospheres today.

These stars have been used to constrain the properties of the first stars (e.g., Limongi et al. 2003; Meynet et al. 2006; Heger & Woosley 2010; Tominaga et al. 2014), the formation sites of early low-mass stars (e.g., Karlsson et al. 2013; Cooke & Madau 2014; Smith et al. 2015), and their formation mechanisms (Frebel et al. 2007a; Schneider et al. 2012; Ji et al. 2014). Moreover, they provide key information on the production of the first elements that ushered in the chemical evolution of the universe (Frebel & Norris 2015). Clearly, these stars are at the heart of stellar archeology and of vital importance to near-field cosmology. Accordingly, several efforts are underway to uncover additional most iron-poor stars (Keller et al. 2007; Caffau et al. 2013; Schlaufman & Casey 2014; Li et al. 2015), reflecting the wide ranging interest in these ancient stars. This follows the HK survey (Beers et al. 1992), the Hamburg/ESO survey (Frebel et al. 2006; Christlieb et al. 2008), and the Sloan Digital Sky Survey (SDSS) and Sloan Extension for Galactic Understanding and

Exploration (SEGUE) survey (Aoki et al. 2013; Caffau et al. 2013; Bonifacio et al. 2015).

We report the detailed chemical abundances of yet another hyper iron-poor star with $[\text{Fe}/\text{H}] = -5.0$. The low-metallicity nature of SDSS J131326.89–001941.4 (hereafter SD 1313–0019) was initially recognized by Allende Prieto et al. (2015) based on a medium-resolution Baryonic Oscillation Spectroscopic Survey (SDSS-BOSS) spectrum with $R \sim 2000$. The analysis of this spectrum showed the star to have $[\text{Fe}/\text{H}] \lesssim -4.3$ and $[\text{C}/\text{Fe}] = 2.5$, making SD 1313–0019 an ideal target for high-resolution spectroscopic follow-up observations to confirm medium-resolution results and determine additional chemical abundances.

2. OBSERVATIONS

We observed SD 1313–0019 (R.A. = $13^{\text{h}}13^{\text{m}}26^{\text{s}}.89$, decl. = $-01^{\circ}19'41''.4$ (J2000.0), $V = 16.9$) with the MIKE spectrograph (Bernstein et al. 2003) on the *Magellan*-Clay telescope at Las Campanas Observatory on 2015 June 16 and 17. A $0''.7$ slit yields a high spectral resolution of $\sim 28,000$ in the red and $\sim 35,000$ in the blue wavelength regime. The total exposure time was 3 hr, although the seeing degraded during the second half of the observations.

Data reductions were carried out with the MIKE Carnegie Python pipeline (Kelson 2003).³ The resulting signal-to-noise ratio per pixel is 45 at $\sim 4700 \text{ \AA}$, 40 at $\sim 5200 \text{ \AA}$, and 55 at $\sim 6000 \text{ \AA}$. Radial velocity measurements yield 274.6 km s^{-1} . This is consistent with the value of $268 \pm 4 \text{ km s}^{-1}$ from the initial SEGUE spectrum (Allende Prieto et al. 2015) from 2008 July 5, but different from the value of $242 \pm 4 \text{ km s}^{-1}$ from the BOSS spectrum from 2014 March 11. We checked our radial velocity zero point with observations of G64–12 obtained on

* This paper includes data gathered with the 6.5 m *Magellan* Telescopes located at Las Campanas Observatory, Chile.

³ Available at <http://obs.carnegiescience.edu/Code/python>.

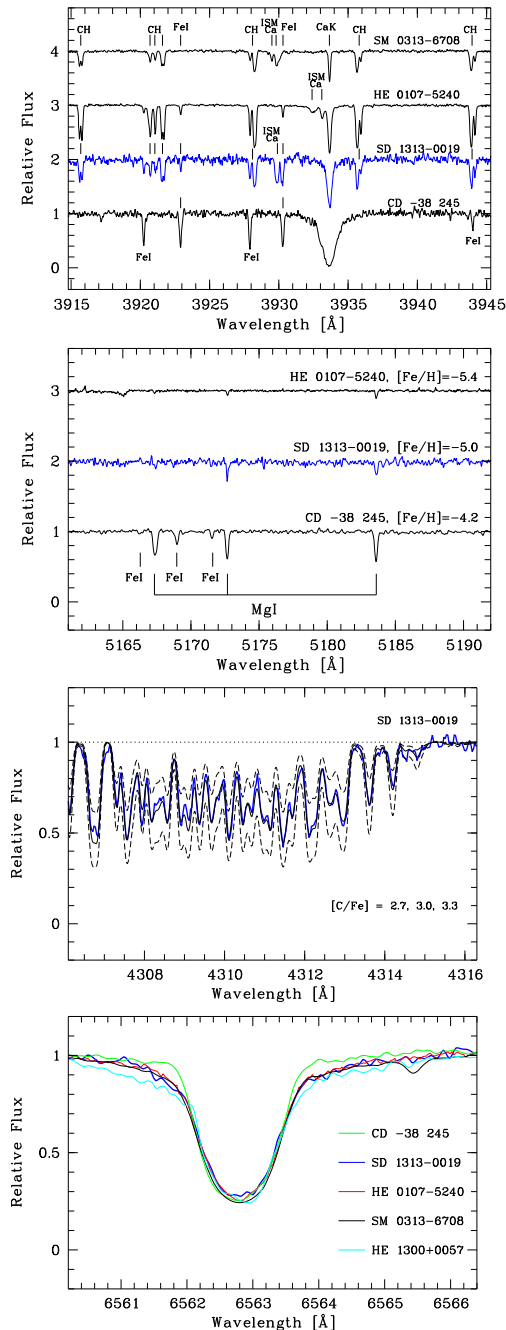


Figure 1. Portions of the *Magellan*/MIKE spectrum of SD 1313–0019 in comparison with other iron-poor stars near the Ca II K line at 3933 Å (top), around the Mg b lines around 5180 Å (second panel), the G-band near 4313 Å (third panel), and the H α line (bottom). Some absorption lines are indicated.

the same night as SD 1313–0019. Its heliocentric radial velocity of 443.0 km s^{−1} agrees extremely well with values in the literature. As already suggested by Allende Prieto et al. (2015), our data support SD 1313–0019 being a member of a binary system, although additional measurements are required to verify this.

In Figure 1, we show several representative portions of the spectrum around the Ca II K line at 3933 Å, the G-bandhead at 4313 Å, and the Mg b lines at 5170 Å. We also show the H α line in comparison with several other stars.

3. CHEMICAL ABUNDANCE ANALYSIS

3.1. Stellar Parameters

We determined the stellar parameters spectroscopically, following the procedure outlined in Frebel et al. (2013). For that, we measured equivalent widths and carried out spectrum synthesis for blended features and to determine upper limits of elements with no detected lines using custom-made software (Casey 2014). The equivalent widths are presented in Table 1. We used a 1D plane-parallel model atmosphere with α -enhancement (Castelli & Kurucz 2004) and a version of the MOOG analysis code that accounts for Rayleigh scattering (Snedden 1973; Sobeck et al. 2011). The abundances are computed under the assumption of local thermodynamic equilibrium (LTE). We derive an effective temperature of $T_{\text{eff}} = 5170$ K after applying the temperature correction (see Frebel et al. 2013). We estimate an uncertainty of ~ 150 K given that we only have 37 Fe I lines available.

This is somewhat cooler than the results of Allende Prieto et al. (2015), who find values ranging from 5250 to 5670 K, but adopt a value of ~ 5300 K. To investigate reasons for these differences, we visually compared the Balmer line strengths of SD 1313–0019 in our spectrum to those of stars with a similar temperature. As can be seen in Figure 1 (bottom panel), the shape of the H α line of SD 1313–0019 agrees very well with those of HE 0107–5240 ($T_{\text{eff}} = 5100$ K; Christlieb et al. 2004) and SM 0313–6708 ($T_{\text{eff}} = 5125$ K; Keller et al. 2014), but not with that of the warmer HE 1300+0057 ($T_{\text{eff}} = 5450$ K; Frebel et al. 2007b) or the cooler CD–38 245 ($T_{\text{eff}} = 4800$ K; Christlieb et al. 2004).

In addition, we repeated our spectroscopic analysis to see if $T_{\text{eff}} = 5300$ K can be supported. Within our equivalent width measurement uncertainties, $T_{\text{eff}} = 5300$ K also satisfies the excitation equilibrium. We thus decided to adopt a temperature of 5200 K, rather than 5100 K, following the Balmer line comparison. Both are consistent with our initial spectroscopic result.

Since no Fe II lines were detected, we adopted a surface gravity from an isochrone. We use one with $[\text{Fe}/\text{H}] = -3.0$ (Kim et al. 2002), but one with $[\text{Fe}/\text{H}] = -2.0$, following the overall metallicity of the star, would essentially give the same result. Our final stellar parameters are $T_{\text{eff}} = 5200 \pm 150$ K, $\log g = 2.6 \pm 0.5$, $v_{\text{micr}} = 1.8 \pm 0.3$ km s^{−1}, and $[\text{Fe}/\text{H}] = -5.0 \pm 0.1$.

3.2. Chemical Abundances and Measurement Uncertainties

Chemical abundances were determined for 10 elements and upper limits of an additional 7 elements. The final abundance ratios $[\text{X}/\text{Fe}]$ are calculated using the solar abundances of Asplund et al. (2009). Our final abundances are listed in Table 2 and shown in Figure 2. We now briefly comment on each element abundance.

Lithium was not detected. Its upper limit $A(\text{Li}) < 0.8$ is consistent with SD 1313–0019 being at the base of the red giant branch, having begun to destroy its surface lithium abundances.

Carbon abundance was determined from the CH G-bandhead at 4313 Å and an additional CH feature at 4323 Å, using the new linelist by Masseron et al. (2014). The best-fit synthetic spectrum is shown in Figure 1. Due to the relatively unevolved nature of SD 1313–0019, the carbon abundance does not need to be corrected for evolutionary status (Placco et al. 2014).

Table 1
Equivalent Width Measurements

Element	λ (Å)	χ (eV)	$\log gf$ (dex)	EW (mÅ)	$\log \epsilon$ (dex)
Li I	6707.7	0.00	0.170	syn	<0.80
CH	4313	syn	6.44
CH	4323	syn	6.34
N (CN) ^a	3883	syn	6.29
Na I	5895.92	0.00	-0.19	9.7	1.61
Mg I	3829.36	2.71	-0.21	47.6	3.17
Mg I	3832.30	2.71	0.27	66.9	3.00
Mg I	3838.29	2.72	0.49	73.6	2.91
Mg I	5183.60	2.72	-0.24	42.4	3.03
Mg I	5172.68	2.71	-0.45	34.5	3.09
Al I	3961.52	0.01	-0.34	20.8	1.34
Si I	3905.52	syn	<2.72
Ca I	4226.73	0.00	0.24	54.1	1.59
Ca II	3933.66	0.00	0.11	390.1	1.73
Sc II	4246.82	syn	-1.54
Ti II	3759.29	0.61	0.28	50.5	0.33
Ti II	3761.32	0.57	0.18	47.5	0.32
Mn I	4030.75	0.00	-0.48	<16.6	<0.66
Fe I	3878.57	0.09	-1.38	45.2	2.54
Fe I	3886.28	0.05	-1.08	58.3	2.45
Fe I	3887.05	0.91	-1.14	13.8	2.47
Fe I	3895.66	0.11	-1.67	28.2	2.51
Fe I	3899.71	0.09	-1.52	40.1	2.57
Fe I	3902.95	1.56	-0.44	18.1	2.63
Fe I	3920.26	0.12	-1.73	32.2	2.66
Fe I	3922.91	0.05	-1.63	30.4	2.45
Fe I	4045.81	1.49	0.28	45.7	2.41
Fe I	4063.59	1.56	0.06	31.1	2.42
Fe I	4071.74	1.61	-0.01	27.3	2.47
Fe I	4132.06	1.61	-0.68	8.3	2.51
Fe I	4202.03	1.49	-0.69	12.0	2.56
Fe I	4271.76	1.49	-0.17	28.5	2.50
Fe I	4325.76	1.61	0.01	28.9	2.46
Fe I	4383.55	1.48	0.20	40.5	2.35
Fe I	4404.75	1.56	-0.15	20.2	2.35
Fe I	4415.12	1.61	-0.62	9.8	2.50
Fe I	3840.44	0.99	-0.50	44.1	2.64
Fe I	3841.05	1.61	-0.04	25.7	2.49
Fe I	3856.37	0.05	-1.28	59.2	2.67
Fe I	3859.91	0.00	-0.71	81.4	2.58
Fe I	3490.57	0.05	-1.11	56.0	2.56
Fe I	3758.23	0.96	-0.01	57.9	2.40
Fe I	3763.79	0.99	-0.22	52.4	2.53
Fe I	3767.19	1.01	-0.39	44.8	2.57
Fe I	3787.88	1.01	-0.84	18.5	2.45
Fe I	3815.84	1.48	0.24	44.9	2.46
Fe I	3820.43	0.86	0.16	70.5	2.39
Fe I	3824.44	0.00	-1.36	55.2	2.62
Fe I	3825.88	0.91	-0.02	63.6	2.46
Fe I	3827.82	1.56	0.094	35.7	2.51
Fe I	3618.77	0.99	-0.00	59.5	2.55
Fe I	3647.84	0.92	-0.14	53.6	2.42
Fe I	3719.94	0.00	-0.42	82.6	2.37
Fe I	3743.36	0.99	-0.79	30.2	2.67
Co I	3873.12	0.43	-0.66	<27.4	<1.70
Ni I	3858.30	0.42	-0.95	18.1	1.58
Ni I	3524.54	0.03	0.01	69.8	1.47
Ni I	3807.14	0.42	-1.22	20.0	1.91
Zn I	4810.53	4.08	-0.14	<2.7	<1.45
Sr II	4215.52	0.00	-0.18	<8.0	<-2.41
Ba II	4554.03	0.00	syn	<6.8	<-2.60

Note.^a Holding the C abundance fixed at $\log \epsilon(\text{C}) = 6.39$.**Table 2**
Magellan/MIKE Chemical Abundances of SD 1313-0019

Species	N	$\log \epsilon(X)$	σ	[X/H]	[X/Fe]
Li (Syn.)	1	<0.80
C (Syn.)	2	6.39	0.28	-2.04	2.96
N (Syn.)	1	6.29	0.40	-1.54	3.46
Na I	1	1.61	0.15	-4.63	0.37
Mg I	5	3.04	0.10	-4.56	0.44
Al I	1	1.34	0.30	-5.11	-0.11
Si (Syn.)	1	<2.72	...	<-4.79	<0.21
Ca I	1	1.59	0.10	-4.75	0.25
Ca II	1	1.73	0.20	-4.61	0.39
Sc (Syn.)	1	-1.54	0.30	-4.69	0.31
Ti II	2	0.33	0.10	-4.62	0.37
Mn I	1	<0.66	...	<-4.77	<0.23
Fe I	36	2.50	0.10	-5.00	0.00
Co I	1	<1.70	...	<-3.29	<1.71
Ni I	3	1.65	0.20	-4.57	0.43
Zn I	1	<1.45	...	<-3.11	<1.89
Sr II	1	<-2.41	...	<-5.28	<-0.28
Ba II	1	<-2.60	...	<-4.78	<0.22

We measured just the 5895 Å line of Na, with the other line at 5885 Å being distorted. There is excellent agreement between the blue Mg triplet and green Mg b lines. Only the Al 3961 Å line was used because the other one available, at 3944 Å, is too heavily blended with CH. We obtained an upper limit for Si from synthesis of the 3905 Å line, which is blended with a molecular CH line. Ca abundances were derived from the Ca I line at 4226 Å and the Ca II K line. The abundances differ by 0.15 dex, with a higher Ca II abundance. With the Ca II K line having an equivalent width of 390 mÅ, we regard it merely as confirmation of the Ca I abundance. We also resolve at least one component of interstellar Ca blueward of the Ca II K line. This was already noticed by Allende Prieto et al. (2015).

One weak Sc line at 4246 Å was tentatively detected, and it is blended with CH. Ti abundance was determined from two Ti lines, yielding good agreement. Ni abundance was determined from three lines. Upper limits for Mn, Co, Zn, Sr, and Ba were determined from the lines at 4030 Å, 3873 Å, 4810 Å, 4077 Å, and 4554 Å, respectively.

Regarding abundance uncertainties, we determined random measurement uncertainties from the standard deviation when more than one line was measured, although we adopt a nominal minimum value of 0.1 dex. For elements with just one line, we assign uncertainties based on abundance changes due to varying the continuum placement. These uncertainties are listed in Table 2. Concerning systematic uncertainties, we re-determined the abundances after changing each of the stellar parameters by their uncertainty while holding the others fixed. The total uncertainties ($\sigma_{\text{rand}} + \sigma_{\text{sys}}$) for most elements are about 0.2 dex and 0.4 dex for [C/Fe] given its temperature sensitivity.

4. DISCUSSION

4.1. Origin of the Abundance Signature of SD 1313-0019 and Other CEMP Stars with [Fe/H] $\lesssim -5.0$

SD 1313-0019 is a hyper iron-poor CEMP star with [C/Fe] = 3.0. Only four stars are currently known with lower [Fe/H] values, and only six other stars have [C/Fe] ratios of [C/Fe] $\gtrsim 3.0$. SD 1313-0019 thus contributes to the 100% CEMP star fraction at the lowest iron abundances (Placco

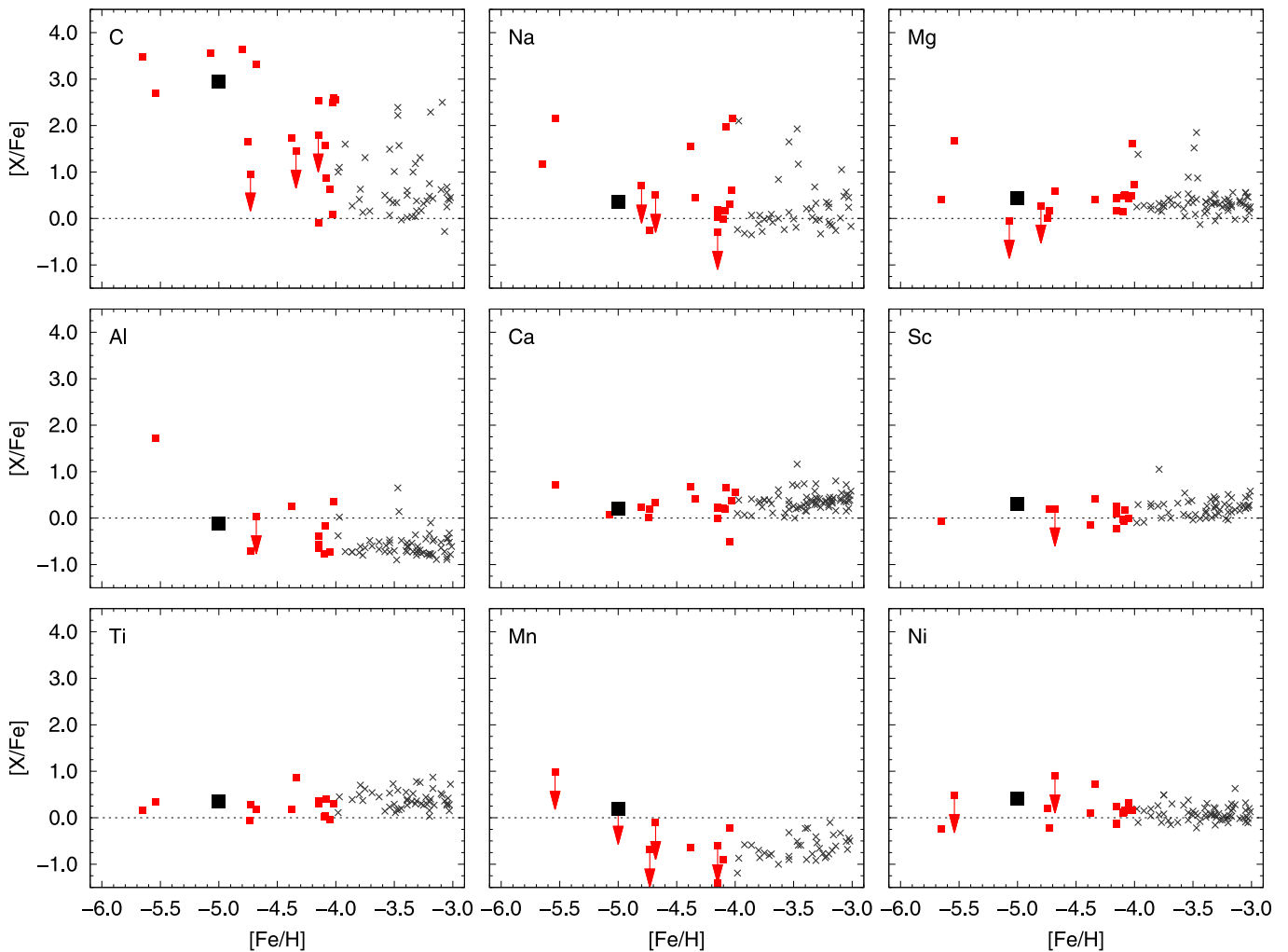


Figure 2. Abundance ratios ($[X/Fe]$) as a function of metallicity ($[Fe/H]$) for various elements detected in SD 1313–0019 (black square) and other halo stars (small red squares for stars with $[Fe/H] \leq -4.0$, otherwise black crosses; Yong et al. 2013 and references in Placco et al. 2015).

et al. 2014). The carbon present in the birth gas clouds may have originated in rotating massive stars that ejected strong stellar winds (e.g., Meynet et al. 2006) in fallback supernovae (e.g., Tominaga et al. 2014) or by two supernovae (e.g., Limongi et al. 2003). See Frebel & Norris (2015) for an extensive discussion.

Alternatively, mass transfer from an erstwhile AGB binary companion might be responsible for the observed high $[C/Fe]$ ratio, given its alleged radial velocity variation. Large amounts of s-process elements would also be expected, such as $[Ba/Fe] > 1.0$, typical for s-process stars (e.g., Placco et al. 2013). This is, however, currently ruled out by its upper limit of $[Ba/Fe] < 0.2$.

4.2. Constraining Population III Star Properties

We now present an example analysis of the abundance pattern of SD 1313–0019 using theoretical model predictions of supernova yields from single non-rotating massive Pop III stars. While other yields could also be used, due to space constraints, we restrict ourselves to the Heger & Woosley (2010) fallback (S4) models⁴ that comprise 120 models with masses from 10 to $100 M_{\odot}$, covering explosion energies from

0.3×10^{51} erg to 10×10^{51} erg. For each energy, there are models with different (fixed) mixing amounts (see Tables 8 and 9 of Heger & Woosley 2010). The mass cut is fixed at all times and assumed to take place at the base of the oxygen burning shell, where the piston is placed.

We use their publicly available χ^2 matching algorithm to determine which model fits our abundances best. The fitting algorithm assumes Sc and Cu are lower limits (generally, Sc is underproduced by the yields), and it ignores Li, Cr, and Zn by default. For both Sc and Cr, Heger & Woosley (2010) assume unaccounted for, additional production sites. Any apparent discrepancy should thus be disregarded.

Results are shown in Figure 3. Fitting the abundance pattern (top left panel) yields a progenitor mass of $27 M_{\odot}$ and a low explosion energy of 0.3×10^{51} erg, although the quality of the fit is only moderate. This could partly be due to our high C and N abundances. Given that 3D effects for abundances determined from molecular features (CH, NH, CN) can be >1 dex, this leaves 1D LTE abundances overestimated compared to those from 3D or time-averaged ($\langle 3D \rangle$) model atmospheres (e.g., Magic et al. 2013).

For example, for the CN feature, Spite et al. (2013) found 3D N abundances to be as much as 2.4 dex lower than 1D values. Therefore, we modified our C and N abundances to investigate

⁴ Accessible at <http://starfit.org>.

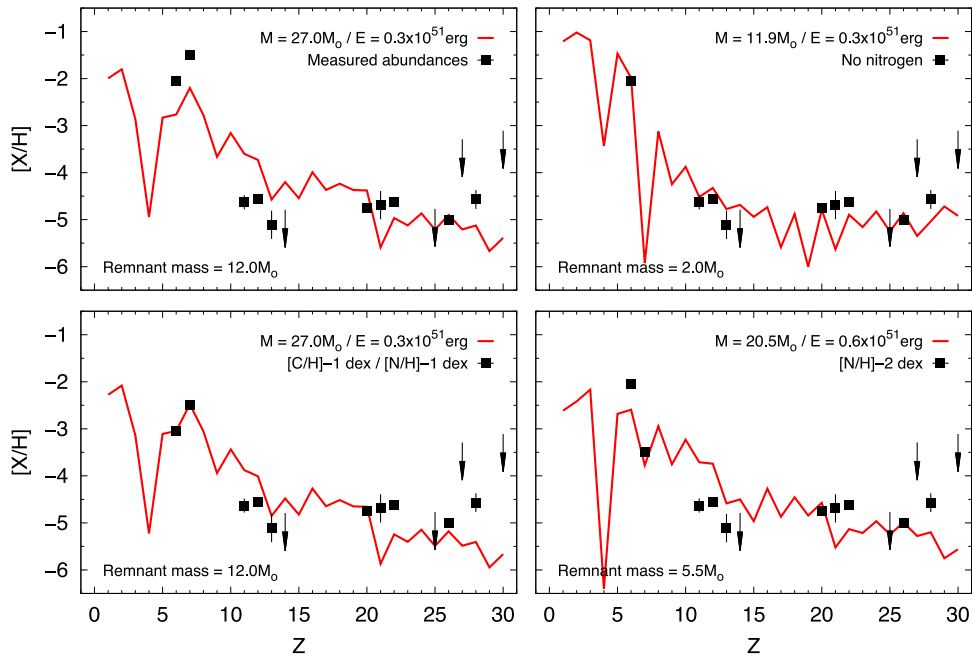


Figure 3. Abundance ratios $[X/H]$ of SD 1313–0019 as a function of atomic number. Four variations on the abundances are shown (see the upper right corners). The solid lines are the best fits for each abundance set using the S4 yields (Heger & Woosley 2010). The resulting model mass and energy are also shown in the upper right and the remnant mass in the lower left. Arrows represent upper limits. See the text for discussion.

potential 3D effects. This follows Placco et al. (2015), who demonstrate that the quality of the match between the star’s abundance pattern to the yields is highly sensitive to the N abundance. To illustrate this issue, the bottom left panel of Figure 3 shows the abundance pattern with $[C/H]$ and $[N/H]$ each reduced by 1 dex. There is no change in the progenitor model, but C and N are now fit well. There is no change for the remaining elements.

To further illustrate the dependence of the best-fit result on the N abundance, we reduced $[N/H]$ by 2 dex but kept the original $[C/H]$ abundance. The progenitor properties changed only slightly: $20 M_{\odot}$ and 0.6×10^{51} erg and, again, an improved fit (bottom right panel). This test simulates the Spite et al. suggestion of a reduced N abundance (when derived from CN). In fact, a lower N value agrees with the upper limit derived from NH lines at 3360 Å. For completeness, we also determine the best fit after excluding the N abundance from the observed pattern (top right panel). The progenitor mass is rather different then, with $12 M_{\odot}$ in line with findings by Placco et al. (2015).

We conclude that the progenitor of SD 1313–0019 had a mass of 20 to $30 M_{\odot}$, was of low explosion energy, and experienced a mixing and fallback episode that led to a high $[C/Fe]$ yield. Future work exploring more details of the mixing and fallback supernovae or alternate production scenarios (Limongi et al. 2003; Meynet et al. 2006) may be able to more closely reproduce the star’s light element abundances.

Another aspect to consider are the observed neutron-capture element abundances and upper limits in the most iron-poor stars. With $[Sr/H] < -5.3$ and $[Ba/H] < -4.8$, SD 1313–0019 possesses extremely low neutron-capture abundances, which are among the lowest ever observed in halo stars (e.g., see Figure 8 in Frebel et al. 2014). Interestingly, these abundance levels strongly resemble those of the stars in the Segue 1 ultra-faint dwarf galaxy (Frebel et al. 2014). This might suggest that SD 1313–0019 formed in a system not too

dissimilar from Segue 1, which is characterized by its uniquely low neutron-capture element content.

More generally, the low Sr and Ba values of SD 1313–0019 extend the decreasing abundance trends of halo stars with decreasing $[Fe/H]$ down to $[Fe/H] = -5.0$. The upper limits of $[Sr/H]$ and $[Ba/H]$ suggest that neutron-capture elements were not made in every first-generation star. This could imply that neutron-capture processes are mass or rotation dependent and only happen in certain mass ranges, such as the s-process in massive rotating low-metallicity stars (Pignatari et al. 2008). Broadly, this would imply a variety of progenitor masses because HE 1327–2326, with $[Fe/H] = -5.6$, has a much larger Sr abundance ($[Sr/H] \sim -4.7$) in contrast to SD 1313–0019. However, current abundance fitting of supernova yields only take into account elements up to Zn, and those results suggest that the progenitors of $[Fe/H] \lesssim -5.0$ stars have a relatively narrow mass range (Placco et al. 2015). Additional iron-poor stars and especially more extensive nucleosynthesis prediction, particularly for neutron-capture element abundances, are needed to fully understand the observed signatures. Nevertheless, it is becoming clear that neutron-capture elements have the potential to strongly constrain progenitor properties.

4.3. The Formation Sites and Mechanisms of the First Low-mass Stars

The first Pop II stars formed in either $\sim 10^6 M_{\odot}$ minihalos or $\sim 10^8 M_{\odot}$ atomic cooling halos. Either formation site is possible, but if the large observed $[C/Fe]$ ratios originated from low energy, faint supernovae, this suggests that minihalos are the preferred formation site of CEMP stars (Cooke & Madau 2014) or even externally enriched minihalos (Smith et al. 2015). However, even if several 10^{51} erg core-collapse supernovae explode in a single minihalo, hydrodynamic simulations with cosmological initial conditions have found

that metals expelled by Pop III stars are retained and second-generation stars form (Ritter et al. 2015). Comparing the latter scenario to models of chemical enrichment suggests that a majority of Pop III supernovae may have provided the carbon enhancement in the abundance signatures of the most iron-poor stars (Ji et al. 2015).

Second-generation star formation may also have occurred in chemically homogeneous clusters (Bland-Hawthorn et al. 2010; Ritter et al. 2015), with two low-mass stars from the same birth gas cloud ending in the stellar halo. In this context, it is interesting to note the remarkably similar abundance patterns of SD 1313–0019 and HE 0557–4840 (Norris et al. 2007). They have different C and N abundances, which could potentially be brought into closer agreement by future NLTE and/or 3D corrections. However, without dynamical information, it cannot be excluded that these two stars formed from distinct supernovae that had produced similar abundance patterns.

Low-mass star formation may be facilitated by atomic carbon and oxygen providing a cooling channel for the primordial gas to sufficiently fragment (Bromm & Loeb 2003). An alternate channel is dust thermal cooling (e.g., Schneider et al. 2012). Both mechanisms can be tested with observational criteria (Frebel et al. 2007a; Ji et al. 2014). The carbon abundance of SD 1313–0019 is $[C/H] \sim -2.0$, easily satisfying the D_{trans} criterion for low-mass star formation through atomic line cooling (Frebel et al. 2007a). This star also has a low silicon abundance $[Si/H] \lesssim -4.8$. If dust in the early universe was predominantly silicates, it could not have formed from standard dust cooling (Ji et al. 2014). Only if carbon dust is able to form or grain growth is important, then dust cooling could have catalyzed SD 1313–0019’s formation (Chiaki et al. 2015).

4.4. About Future Searches for CEMP Stars with $[Fe/H] \lesssim -4.0$

While Allende Prieto et al. (2015) found $[Fe/H] = -4.3$ for SD 1313–0019 based on a medium-resolution spectrum ($R \sim 2000$), we find a significantly lower metallicity even when taking the effective temperature differences into account. Using 5378 K, we find $[Fe/H] = -4.82$. The Ca II K line, on which the medium-resolution value was based, is blended with a double-peaked carbon feature at 3935.5 Å. After smoothing our spectrum to a comparable resolution, we recovered the quoted equivalent width of 640 mÅ of Allende Prieto et al. (2015). Our corresponding abundance is $[Ca/H] \sim -4.0$, which agrees with their $[Fe/H] = -4.3$, assuming $[Ca/Fe] \sim 0.3$.

Since the most iron-poor stars are likely to be carbon enhanced, they display strong CH features throughout the blue part of the spectrum, including near the Ca II K line. Examples include HE 0107–5240 (Christlieb et al. 2002) and SM0313–6708 (Keller et al. 2014), where the equivalent width of the combined Ca II K–CH_{3935.5} feature is about twice that of the Ca II K line alone (see Figure 1). In fact, the discrepancy between medium- and high-resolution spectra of nine of the most iron-poor stars varies from -0.5 to -1.75 dex. It is thus impossible for this population of stars to obtain an accurate $[Fe/H]$ estimate from the Ca K II unless this effect is taken into account.

With an independent C abundance (e.g., from the G-band, measurable in medium-resolution spectra) and approximate

stellar parameters, it should be possible to predict the contribution of the CH feature at 3935.5 Å and subtract it from the equivalent width of the Ca II K line. This will become particularly important for both spectroscopic and narrowband photometric surveys that contain large amounts of fainter metal-poor stars that cannot be followed up with high-resolution spectroscopy. Overestimating the iron abundances of the most iron-poor stars due to this carbon contamination would skew the shape of the metallicity distribution function at its tail end, thus hampering our understanding of the formation of the earliest long-lived stars as well as the stellar halo of the Milky Way.

A.F. and A.P.J. are supported by NSF CAREER grant AST-1255160. A.F. is also partially supported by the Silverman (1968) Family Career Development Professorship. A.F. and V.M.P. acknowledge partial support for this work from PHY 08-22648; Physics Frontier Center/Joint Institute for Nuclear Astrophysics (JINA) and PHY 14-30152; and Physics Frontier Center/JINA Center for the Evolution of the Elements (JINA-CEE), awarded by the US National Science Foundation. This work made use of NASA’s Astrophysics Data System Bibliographic Services.

Facility: Magellan-Clay (MIKE).

REFERENCES

- Allende Prieto, C., Fernandez-Alvar, E., Aguado, D. S., et al. 2015, *A&A*, **579**, A98
- Aoki, W., Beers, T. C., Lee, Y. S., et al. 2013, *AJ*, **145**, 13
- Asplund, M., Grevesse, N., Sauval, A. J., & Scott, P. 2009, *ARA&A*, **47**, 481
- Beers, T. C., Preston, G. W., & Shectman, S. A. 1992, *AJ*, **103**, 1987
- Bernstein, R., Shectman, S. A., Gunnels, S. M., Mochnacki, S., & Athey, A. E. 2003, *Proc. SPIE*, **4841**, 1694
- Bland-Hawthorn, J., Karlsson, T., Sharma, S., Krumholz, M., & Silk, J. 2010, *ApJ*, **721**, 582
- Bonifacio, P., Caffau, E., Spite, M., et al. 2015, *A&A*, **579**, A28
- Bromm, V., & Loeb, A. 2003, *Natur*, **425**, 812
- Caffau, E., Bonifacio, P., François, P., et al. 2011, *Natur*, **477**, 67
- Caffau, E., Bonifacio, P., Sbordone, L., et al. 2013, *A&A*, **560**, A71
- Casey, A. R. 2014, arXiv:1405.5968
- Castelli, F., & Kurucz, R. L. 2004, arXiv:astro-ph/0405087
- Chiaki, G., Marassi, S., Nozawa, T., et al. 2015, *MNRAS*, **446**, 2659
- Christlieb, N., Bessell, M. S., Beers, T. C., et al. 2002, *Natur*, **419**, 904
- Christlieb, N., Gustafsson, B., Korn, A. J., et al. 2004, *ApJ*, **603**, 708
- Christlieb, N., Schörck, T., Frebel, A., et al. 2008, *A&A*, **484**, 721
- Cooke, R. J., & Madau, P. 2014, *ApJ*, **791**, 116
- Frebel, A., Aoki, W., Christlieb, N., et al. 2005, *Natur*, **434**, 871
- Frebel, A., Casey, A. R., Jacobson, H. R., & Yu, Q. 2013, *ApJ*, **769**, 57
- Frebel, A., Christlieb, N., Norris, J. E., et al. 2006, *ApJ*, **652**, 1585
- Frebel, A., Johnson, J. L., & Bromm, V. 2007a, *MNRAS*, **380**, L40
- Frebel, A., & Norris, J. E. 2015, arXiv:1501.06921
- Frebel, A., Norris, J. E., Aoki, W., et al. 2007b, *ApJ*, **658**, 534
- Frebel, A., Simon, J. D., & Kirby, E. N. 2014, *ApJ*, **786**, 74
- Heger, A., & Woosley, S. E. 2010, *ApJ*, **724**, 341
- Ji, A. P., Frebel, A., & Bromm, V. 2014, *ApJ*, **782**, 95
- Ji, A. P., Frebel, A., & Bromm, V. 2015, *MNRAS*, submitted (arXiv:1508.06137)
- Karlsson, T., Bromm, V., & Bland-Hawthorn, J. 2013, *RvMP*, **85**, 809
- Keller, S. C., Bessell, M. S., Frebel, A., et al. 2014, *Natur*, **506**, 463
- Keller, S. C., Schmidt, B. P., Bessell, M. S., et al. 2007, *PASA*, **24**, 1
- Kelson, D. D. 2003, *PASP*, **115**, 688
- Kim, Y.-C., Demarque, P., Yi, S. K., & Alexander, D. R. 2002, *ApJS*, **143**, 499
- Li, H., Aoki, W., Zhao, G., et al. 2015, arXiv:1506.05684
- Limongi, M., Chieffi, A., & Bonifacio, P. 2003, *ApJL*, **594**, L123
- Magic, Z., Collet, R., Asplund, M., et al. 2013, *A&A*, **557**, A26
- Masseron, T., Plez, B., van Eck, S., et al. 2014, *A&A*, **571**, A47
- Meynet, G., Ekström, S., & Maeder, A. 2006, *A&A*, **447**, 623
- Norris, J. E., Christlieb, N., Korn, A. J., et al. 2007, *ApJ*, **670**, 774
- Pignatari, M., Gallino, R., Meynet, G., et al. 2008, *ApJL*, **687**, L95
- Placco, V. M., Frebel, A., Beers, T. C., et al. 2013, *ApJ*, **770**, 104

- Placco, V. M., Frebel, A., Beers, T. C., & Stancliffe, R. J. 2014, [ApJ](#), **797**, 21
- Placco, V. M., Frebel, A., Lee, Y. S., et al. 2015, [ApJ](#), **809**, 136
- Ritter, J. S., Sluder, A., Safrank-Shrader, C., Milosavljevic, M., & Bromm, V. 2015, [MNRAS](#), **451**, 1190
- Schlaufman, K. C., & Casey, A. R. 2014, [ApJ](#), **797**, 13
- Schneider, R., Omukai, K., Limongi, M., et al. 2012, [MNRAS](#), **423**, L60
- Smith, B., Wise, J., O'Shea, B., Norman, M., & Khochfar, S. 2015, [MNRAS](#), **452**, 2822
- Snedden, C. A. 1973, PhD thesis, Univ. Texas
- Sobeck, J. S., Kraft, R. P., Sneden, C., et al. 2011, [AJ](#), **141**, 175
- Spite, M., Caffau, E., Bonifacio, P., et al. 2013, [A&A](#), **552**, A107
- Tominaga, N., Iwamoto, N., & Nomoto, K. 2014, [ApJ](#), **785**, 98
- Yong, D., Norris, J. E., Bessell, M. S., et al. 2013, [ApJ](#), **762**, 26